Electrochimica Acta 449 (2023) 142210

Contents lists available at ScienceDirect

Electrochimica Acta

journal homepage: www.journals.elsevier.com/electrochimica-acta

Energy storage enhancement of $Li_xMn_{1.8}Ti_{0.2}O_4$@N-doped graphene oxide in organic and ionic liquid electrolytes

Nerly Mosquera [a], Susana Chauque [b,1], Roberto M. Torresi [b,*], Jorge A. Calderón [a,*]

[a] Centro de Investigación, Innovación y Desarrollo de Materiales—CIDEMAT, Universidad de Antioquia, Cr. 53 No 61 – 30, Torre 2, Lab. 330, Medellín, Colombia
[b] Departamento de Química Fundamental, Instituto de Química, Universidade de São Paulo, Av. Prof. Lineu Prestes, 748, São Paulo, SP 05508-000, Brazil

ARTICLE INFO

Keywords:
Spinel positive electrode
Lithium-ion batteries
Ionic liquids
High potential
High temperature

ABSTRACT

Spinel-type $Li_{1-x}Mn_2O_4$ material is a promising positive electrode material for lithium-ion batteries. This material presents 3D diffusion channels through the structure, allowing for the rapid diffusion of lithium ions during charge/discharge processes. Given its relevant properties, such as a theoretical specific capacity of 149 mA h g^{-1} and high working potential, we propose $Li_xMn_{1.8}Ti_{0.2}O_4$@N-doped graphene oxide ($x \leq 1$) as a superior positive electrode material for lithium-ion battery applications. In organic media, the spinel showed excellent Li storage performance due to the incorporation of a conductive carbonaceous matrix (using 1,10 phenanthroline as a graphene precursor). We obtained a specific capacity of 139 mA h g^{-1}, which represented 81% charge retention after 70 cycles. Furthermore, taking advantage of the high working potential of this material, we studied the Li storage capacity using ionic liquids as electrolyte solvents. High rate cycling at high temperatures is essential for their practical applications in extreme environments. In this work, we performed rate capability experiments at different temperatures, obtaining the best response at 40 °C with a specific capacity of 117 mA h g^{-1} at an applied current density of 1 C.

1. Introduction

Lithium-ion batteries (LIBs) have received worldwide attention as a power source for transport applications in electric vehicles and hybrid electric vehicles and massive energy storage facilities [1,2]. However, their large-scale application is hindered by severe safety concerns when the cells are exposed to harsh mechanical, thermal, or electrical conditions [3]. Much effort has been directed toward the development of devices that present high energy density, high-rate capability, cycling performance, environmental friendliness, low cost, and higher enhanced safety, which is a critical fundamental to future advancement of LIBs [4].

In particular, spinel-type $Li_{1-x}Mn_2O_4$ is a potential positive electrode material that is proposed as an alternative for next-generation LIBs. This material presents a specific capacity of 148 mA h g^{-1} and a higher working potential (4.1 V) than other positive materials, such as $LiCoO_2$ (4.0 V) and $LiFePO_4$ (3.5 V) [5,6]. Additionally, 3D diffusion channels are present through the spinel structure, allowing the rapid diffusion of lithium ions [7,8]. Nevertheless, the classic $Li_{1-x}Mn_2O_4$ spinel exhibits a structural transformation during charge/discharge processes due to Jahn-Teller distortion, leading to poor cycling stability [9]. An effective strategy for solving this problem involves doping or substituting with transition metals such as Fe, Co, Al, V, Nb and Ti [10]. In particular, doping with Ti has been widely explored for this purpose, since the bonding energy of Ti-O (662 kJ mol^{-1}) is higher than that of Mn-O (402 kJ mol^{-1}); thus, the stability of the structure and the cyclability of the material could be improved [11]. Additionally, partial substitution with Ti increases the unit cell size and enhances the potential of lithium-ion diffusion [12]. However, the spinel $LiMn_{2-x}Ti_xO_4$ phase exhibits a low capacity for the electrochemical inactivity of Ti in the potential window of 3.0–4.6 V [8]. There are few studies showing the effect of partial Ti substitution in $LiMn_2O_4$ spinel as a positive electrode in LIBs. For instance, *Kesavan* et al. showed that $LiMn_{1.8}Ti_{0.2}O_4$ spinel (Mn/Ti:9) exhibited enhanced specific capacities of 132 mA h g^{-1} at a current rate of 0.1 C within a potential range of 1.5–4.8 V, which was attributed to the suppression of Jahn–Teller distortion [13]. Recently, we showed that during cycling between 4.6–2.0 V, the $Li_xMn_{2-y}Ti_yO_4$ spinel-type materials suffer undesired structural modifications for the $Mn^{3+}|Mn^{2+}$ transition and the formation of an irreversible tetragonal phase that increases charge transfer resistance [14].

* Corresponding authors.
E-mail addresses: rtorresi@iq.usp.br (R.M. Torresi), andres.calderon@udea.edu.co (J.A. Calderón).
[1] Present address: Istituto Italiano di Tecnologia, Via Morego 30, 16,163 Genova, Italy.

https://doi.org/10.1016/j.electacta.2023.142210
Received 21 June 2022; Received in revised form 12 February 2023; Accepted 9 March 2023
Available online 12 March 2023

Surface modification has been applied to improve the energy density and electrical conductivity of lithium-rich manganese oxides [15,16]. The employment of $LiMn_{2-x}Ti_xO_4$ spinel nanoparticles in combination with conductive materials, such as carbonaceous materials, has attracted attention because it can lead to high capacities and high cyclability properties [17,18]. Recently, several novel electrode structures designs have been developed. For instance, Pyun et al. reported the excellent rate capability of the graphene/$LiMn_{2-x}O_4$ electrode showing a specific capacity of 126 mA h g^{-1} at a current density of 840 mA g^{-1} [19]. Also, *Bao* et al. prepared a $LiMnTiO_4$/MWCNT composite electrode, improving the conductivity of the material and preventing the capacity fading of $LiMnTiO_4$ during the cycling and obtaining a discharge capacity of 77 mA h g^{-1} at a rate of 5 C [20]. Even though surface modification with carbonaceous graphene has been used to enhance the electrochemical properties, sometimes the material stability has been deteriorated by active material contact with the electrolyte solution.

Traditionally, electrolytes composed of a lithium salt, commonly lithium hexafluorophosphate ($LiPF_6$), dissolved in a mixture of organic solvents such as ethylene carbonate (EC), diethyl carbonate (DEC), dimethyl carbonate (DMC), or ethyl methyl carbonate (EMC) and/or propylene carbonate (PC) have been employed for LIB fabrication [3,21]. Although the use of these electrolytes results in good cell performances at potentials less than 4.5 V, the use of high cutoff potentials induces the instability of carbonate-based organic electrolytes and contributes to rapid battery deterioration [22]. Ionic liquids (ILs) have been proposed as a safer alternative solvent for use in electrolytes for LIBs. The properties of IL-based electrolytes make them more thermally and chemically stable, as in turn, they present low volatility and flammability and a wider usable temperature and potential window [21,23]. *Honghe Zheng* et al. investigated the electrochemical properties of a spinel $LiMn_2O_4$ positive electrode in 1.0 mol L^{-1} lithium bis(trifluoromethanesulfonyl)imide (LiTFSI) in trimethylhexylammonium (TMHA) and bis(trifluoromethane)sulfonylimide (TFSI) (LiTFSI/TMHA-TFSI) as an electrolyte at an operating voltage between 3.3 and 4.3 V and a current density of 15.0 mA g^{-1}. The authors obtained a discharge capacity of 108.2 mA h g^{-1} and a coulombic efficiency of 91.4% during the first cycle at room temperature [24]. Most recently, *Hyeon Jeong Lee* et al. presented a positive electrode material, $LiNi_{0.5}Mn_{1.5}O_4$, which used 1.0 mol L^{-1} lithium bis(fluorosulfonyl)imide (LiFSI) in *N*-propyl-*N*-methylpyrrolidinium bis(fluorosulfonyl) imide ($Pyr_{1,3}FSI$) as an IL electrolyte (LiFSI/$Pyr_{1,3}FSI$). The $LiNi_{0.5}Mn_{1.5}O_4$ positive electrode exhibited a rate performance of 106 mA h g^{-1} at 5C and a capacity retention of 89.5% after 100 cycles at 0.2 C within a potential range of 3.5–5.0 V [7]. However, the specific capacity values are limited when the IL-based electrolytes are operated at room temperature and the active materials present a moderate ion conductivity limiting the Li+ diffusion and electron transfer at the surface of the material. A strategy to address the issues related to the low conductivity of IL-based cells is the use of carbon-based composite materials because it can enhance the ion diffusion and improve the structure stability [25,26]. Accordingly, many researchers have focused on improving the electrochemical response from oxides supported on carbonaceous materials.

In the current work we propose the hybrid material $Li_xMn_{1.8}Ti_{0.2}O_4$@N-doped graphene oxide (GO) (where $x \leq 1$) as an alternative of positive electrode against to the expensive and controversial $LiCoO_2$ material for LIBs. We provide a simple method to modify the $Li_{1-x}Mn_{1.8}Ti_{0.2}O_4$ spinel by the incorporation of GO using 1.10 phenanthroline as a precursor of the carbon material. So, the graphene oxide (GO) is directly produced during the synthesis of the active material, providing a more intimate contact between the carbonaceous material and the active spinel particles. In addition, it is shown that the electrochemical performance of the material can be improved if a full cell (as practical application) is operated using an ionic liquid as electrolyte at a moderate temperature of 40 °C.

From a complete structural and morphological characterization of the samples (pristine and hybrid spinel), we obtained a pure crystalline material. Our electrochemical study starts with a complete analysis of the hybrid material on a commercial electrolyte (1.0 mol L^{-1} $LiPF_6$ in ethylene carbonate (EC) and diethyl carbonate (DMC) with a 1:1 vol ratio), showing remarkable enhancement in the cycling stability and a rate capability response due to the presence of the N-doped graphene oxide, of which phenanthroline was the precursor. The $Li_xMn_{1.8}Ti_{0.2}O_4$@N-doped graphene oxide electrode presented an initial capacity of 139.4 mA h g^{-1}, and after 50 cycles, it decayed to 112.1 mA h g^{-1} and then to 104 mA h g^{-1} in the 70th cycle, maintaining a capacity retention of 89%. Taking advantage of the potential range in which our proposed material works, we used IL-based electrolytes (i.e., 1.0 mol L^{-1} LiTFSI in [($Pyr_{1,4}$)(TFSI)]), and we performed the experiments at temperatures higher than 25 °C. The optimum operating temperature for the battery with the IL as the electrolyte in terms of the rate capability response was found to be 40 °C. At 40 °C, our hybrid material presented a pronounced specific capacity of 117 mA h g^{-1} at an applied current of 1 C. The lithium storage properties of $Li_xMn_{1.8}Ti_{0.2}O_4$@N-doped graphene oxide on both electrolytes, the simplicity of its synthesis and the excellent response at high current densities and work temperatures make this material a superior candidate for long-lasting and efficient positive electrodes for LIB applications.

2. Experimental

2.1. Materials

The following reagents (analytical grade) were used to synthesize the active material: lithium acetate dihydrate, $Li(COOH)\cdot 2H_2O$ (Sigma Aldrich; 99%); manganese acetate tetrahydrate, $Mn(CH_3COO)_2\cdot 4H_2O$ (Sigma Aldrich; ≥99%); titanium diisopropoxide bis(acetylacetonate), $[(CH_3)_2CHO]_2Ti(C_5H_7O_2)_2$) (Sigma Aldrich; 75 wt.% in isopropanol); oxalic acid dihydrate, $(COOH)_2\cdot 2H_2O$ (Duksan; ≥99,5%); ethylene glycol, $C_2H_6O_2$ (Panreac); 1,10 phenanthroline, $C_{12}H_8N_2$ (Sigma Aldrich; ≥99%); N-methyl-2-pyrrolidone (Sigma Aldrich; 99.5%); polyvinylidene fluoride, PVdF (MTI technologies); carbon black C65 (MTI technologies); lithium metal foils, Li (Sigma Aldrich, 99.9%); N-butyl-N-ethyl pyrrolidinium N,N-bis(trifluoromethanesulfonyl)imide, $Pyr_{1,4}$TFSI (Io-li-tec; 99.5%); and lithium bis(trifluoromethanesulfonyl)imide, LiTFSI (Sigma Aldrich; 99.5%).

2.2. Synthesis of $Li_xMn_{1.8}Ti_{0.2}O_4$ spinel

Pristine $Li_xMn_{1.8}Ti_{0.2}O_4$ spinel (where $x \leq 1$) was synthesized by a modified sol-gel method according to the method reported in our previous study [14]. Stoichiometric amounts of $Mn(CH_3COO)_2\cdot 4H_2O$, previously dehydrated at 110 °C for 24 h under vacuum, and $LiC_2H_3O_2\cdot 2H_2O$ (5% excess), which was included to compensate for lithium loss during high-temperature calcination, were separately dissolved in absolute ethanol (Scharlau, 99.5%) and methanol (Chemí, 99.8%), respectively. Afterward, oxalic acid dihydrate and ethylene glycol were dissolved in 20 mL of ethanol and continuously stirred at 90 °C. The titanium precursor, $[(CH_3)_2CHO]_2Ti(C_5H_7O_2)_2$, was transferred to the oxalic acid/ethylene glycol mixture. Subsequently, the solutions with the Li and Mn precursors were slowly added simultaneously to the previous mixture with vigorous stirring (ca. 1200 rpm) at 90 °C until a polymerized gel formed. The resultant gel was dried under vacuum at 120 °C for 48 h. The prepared precursor was hand-milled in an agate mortar and subsequently sintered at 650 °C for 12 h at a heating rate of 5.4 °C min^{-1}. The cooling rate was 1.6 °C min^{-1} from 650 °C to 550 °C, and then the material was cooled quickly to obtain the final $Li_xMn_{1.8}Ti_{0.2}O_4$ material.

2.3. Synthesis of $Li_xMn_{1.8}Ti_{0.2}O_4$@N-doped graphene oxide

To prepare the hybrid material, 1,10 phenanthroline was dissolved in the presence of the prepared $Li_xMn_{1.8}Ti_{0.2}O_4$ (in a 60:40 mass

proportion) in absolute ethanol. This mixture was maintained under vigorous stirring for 12 h at room temperature. Afterward, the solvent was carefully evaporated, and the powder was dried overnight at 80 °C. Finally, the solid was annealed at 800 °C for 2 h under nitrogen flux to prevent the oxidation of carbon [27,28].

2.4. Material characterization

The crystal structure of the samples was characterized by X-ray diffraction (XRD) using an X-ray diffractometer (Rigaku Miniflex 600) with a Cu radiation source (ka1/a2) = 1.54178 Å in the range of $10° \leq 2\theta \leq 80°$ with a step size of 0.025° The analysis of crystalline phases was performed using High Score Plus software with the PDF-2 database. The Raman spectra were taken in a Horiba Jobin Yvon (Labram HR) Nikon (BX41) microscope using a laser wavelength of 632 nm, 0.3 D filter, a 50X objective and a sweep range of 100–3000 cm^{-1}. The presence of functional groups in N-doped graphene oxide was confirmed by Fourier transform infrared spectroscopy (FTIR). The spectra were acquired on a Shimadzu Prestige-IR spectrophotometer with an MCT detector, and 64 scans were acquired at a resolution of 4 cm^{-1}. The morphology and size of the synthesized particles were analyzed by scanning electron microscopy (SEM) using JEOL JSM 6490 LV equipment coupled to EDS to determine the atomic composition. The compositions of the active materials and the oxidation states of the elements as well as those of the cathodic electrolyte interface (CEI) formed in different electrolytes were determined by X-ray photoelectron spectroscopy (XPS) analysis using a NAP-XPS Specs Phiobos 150 1D-DLD analyzer. This system incorporates a monochromated Al Kα X-ray source (hν = 1486.7 eV, 13 kV, 100 W). The high-resolution XPS spectra were recorded at a constant pass energy of 90 eV (3 cycles) for the survey spectra and 20 eV (20 cycles) for the high-resolution core level spectra. The specific surface area and the pore-size distribution were measured by BET for N_2 absorption (ASAP 2020 Micromeritics) and pore size analysis.

2.5. Electrochemical characterization

The positive electrodes were fabricated from a slurry containing 80 wt% active materials ($Li_xMn_{1.8}Ti_{0.2}O_4$ and $Li_xMn_{1.8}Ti_{0.2}O_4$@N-doped graphene oxide), 10 wt% carbon black super P, and 10 wt% PVdF binder in NMP as a dispersant. The slurry was cast onto an Al foil as a current collector using a continuous doctor blade coating system and subsequently dried under vacuum at 80 °C overnight. The 2032-type coin cells were assembled inside an Ar-filled MBraun glovebox in which the amount of water and oxygen concentration was below 0.5 ppm. $Li_xMn_{1.8}Ti_{0.2}O_4$ and $Li_xMn_{1.8}Ti_{0.2}O_4$@N-doped graphene oxide, each with a diameter of approximately 12 mm, were used as positive electrodes. Lithium metal foil disks 0.75 mm thick and approximately 10 mm in diameter were used as the counter electrodes, and a glass microfiber (Whatman, grade GF/D) was used as the separator. For the tests in organic solvents, we used commercial LP30. For the experiments with IL as the electrolyte, a solution of 1.0 mol L^{-1} LiTFSI in $[Pyr_{1,4}][TFSI]$ was used. The galvanostatic charge/discharge (GCD) cycling performance was typically performed between 4.6 and 3.0 V at a constant current of 15.0 mA g^{-1}, equivalent to a rate of 1 C, assuming a theoretical specific capacity of 150 mA h g^{-1}. Cyclic voltammetry (CV) experiments were carried out between 3.0 V and 4.6 V at 0.1 mV s^{-1}. For electrochemical impedance spectroscopy (EIS) at different states of charge and discharge, we used a three-electrode Swagelok T cell. We performed the EIS experiments in a frequency range of 10 kHz-9 mHz and recorded 5 data points per decade. Different electrical parameters were obtained from the EIS data fitting analysis using Origin 2019 software. The GCD cycling as well as the CV and EIS experiments of the electrodes were performed using a BioLogic BCS 805 potentiostat/galvanostat. The values of electrical conductivity were obtained using from current vs. potential (i vs. E) measurements in a two-cell terminal. The electrodes were constructed pressing the active material under 10 MPa at room temperature. The thickness and diameter of the samples were measured using a micrometer Mitutoyo IP 65 (0 – 25 mm ± 0.001 mm), and a digital caliper, Mitutoyo, respectively. The experiments were performed in a potentiostat/galvanostat (Solartron Analytical, CellTest System 1470E). Finally, the effect of temperature on the electrochemical behavior was studied by rate capability tests. The spinel $Li_xMn_{1.8}Ti_{0.2}O_4$@N-doped graphene oxide electrode in 1.0 mol L^{-1} LiTFSI/[(Pyr_{14})(TFSI)] electrolyte was investigated at different temperatures (25 °C, 40 °C and 60 °C) using a Binder KB115 drying oven.

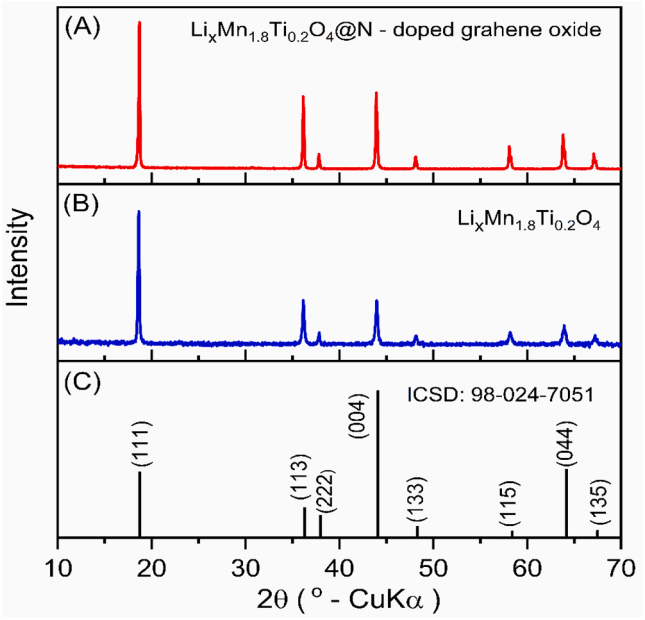

Fig. 1. XRD patterns of the (A) $Li_xMn_{1.8}Ti_{0.2}O_4$@N-doped graphene oxide hybrid material. (B) Pure $Li_xMn_{1.8}Ti_{0.2}O_4$ spinel and (C) ICSD reference pattern.

3. Results and discussion

3.1. Chemical and structural characterization

The XRD patterns of the pure $Li_xMn_{1.8}Ti_{0.2}O_4$ spinel and the hybrid material $Li_xMn_{1.8}Ti_{0.2}O_4$@N-doped graphene oxide are shown in Fig. 1. The shape and intensity of the peaks of the XRD patterns could be indexed as a cubic spinel structure with an Fd-3 m space group (ICSD 98–024–7051), in agreement with a previous study [13]. The patterns showed reflections located at angles 2θ = 18.7°, 36.3°, 37.9°, 44.1°, 48.3°, 58.4°, 64.2° and 67.5° corresponding to the Miller indices of (111), (113), (222), (004), (133), (115), (044) and (135), respectively. According to the diffractogram, the $Li_xMn_{1.8}Ti_{0.2}O_4$@N-doped graphene oxide sample do not exhibit phase transitions or a significant quantity of impurities after annealing at elevated temperatures. Thus, the synthesis procedure performed in this work allows high purity of the sample to be achieved compared to those described in the literature reports [20].

We also confirm that the synthesis method performed do not affect the spinel structure by Raman Spectroscopy. The lattice vibrational modes of the pure $Li_xMn_{1.8}Ti_{0.2}O_4$ and $Li_xMn1.8Ti_{0.2}O_4$@N-doped graphene oxide composite were analyzed. The complete Raman spectrum is presented in Fig. 2(A). In the range between 100 and 800 cm^{-1}, we identified A_{1g}, E_g and three F_{2g} vibrational modes exhibited by spinel-type materials [29], as shown in Fig. 2(A) and (B). The materials present two strong bands at approximately 570 and 640 cm^{-1}, which correspond to the A_{1g} and $F_{2g}^{(1)}$ modes of the symmetric Mn/Ti−O stretching vibrations of the MO_6 octahedron [30]. The symmetric stretching of the Ti–O bonds at the TiO_6 octahedral sites and the Mn–O bonds at the MnO_6 octahedral sites is superimposed on the A_{1g} and F_{2g}

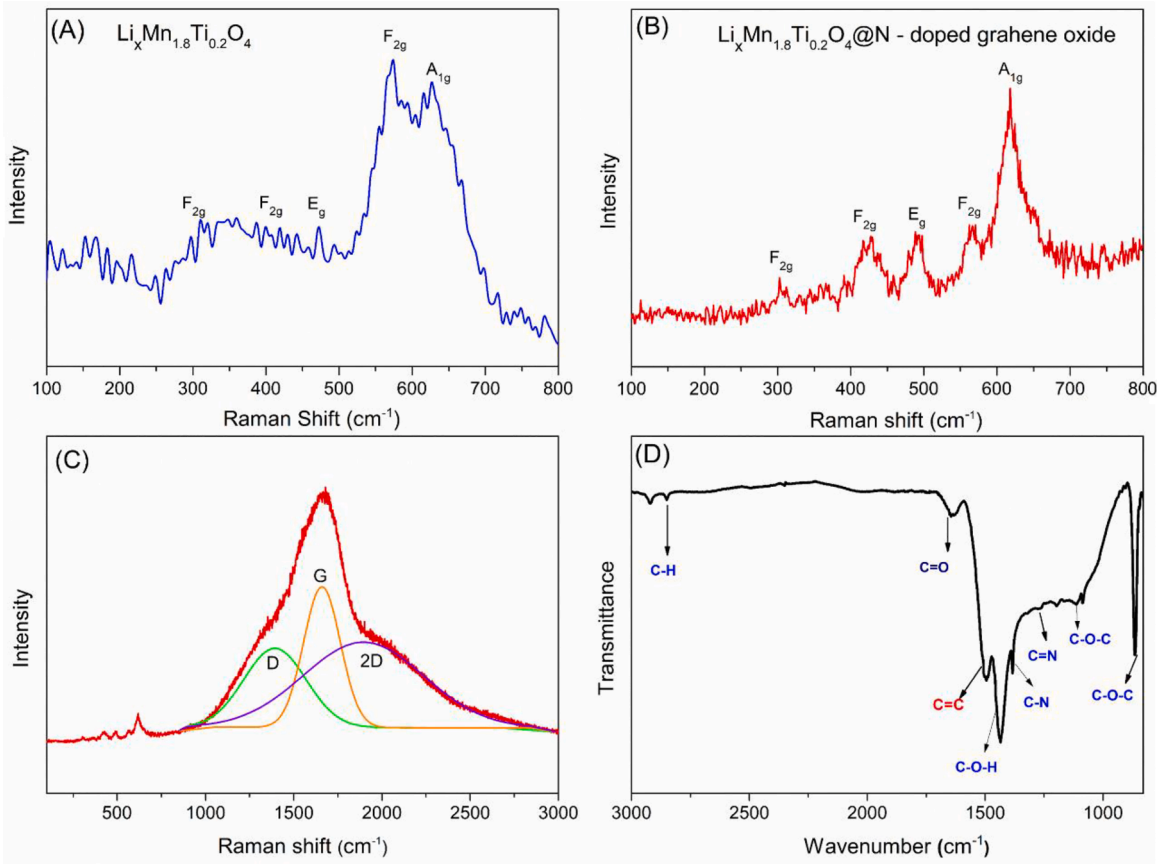

Fig. 2. (A) Raman spectra of $Li_xMn_{1.8}Ti_{0.2}O_4$ and of (B) $Li_xMn_{1.8}Ti_{0.2}O_4$@N-doped graphene oxide shown between 100 and 800 cm^{-1}. (C) Deconvolution of the Raman signal between 800 and 3000 cm^{-1}. (D) FTIR spectrum of the $Li_xMn_{1.8}Ti_{0.2}O_4$@N-doped graphene oxide composite.

bands [29,31]. Similarly, a set of bands with lower intensity is presented between 150 and 520 cm^{-1}, corresponding to the $F_{2g}^{(2)}$, E_g and $F_{2g}^{(3)}$ modes associated with the Li−O symmetric bonding in LiO_4 tetrahedra and the symmetric bonding vibration corresponding to the O-Mn/Ti-O bonds [32]. The Raman spectrum also exhibits a broad, high-intensity band between 800 and 3000 cm^{-1}; this band is related to the carbon

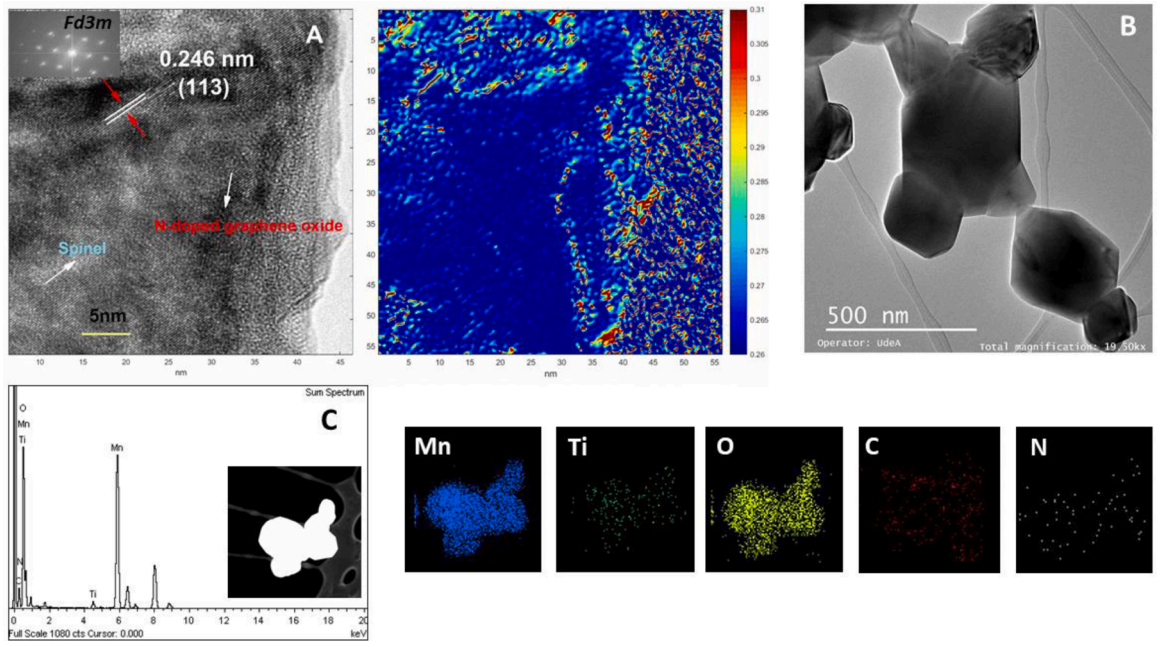

Fig. 3. (A) TEM image of the $Li_xMn_{1.8}Ti_{0.2}O_4$@N-doped graphene oxide composite with fast Fourier transform showing spinel structures with the space group indicated and color box images of the local vector with the D-spacing (color scale bar of D-spacing in nm), (B) HR-TEM and (C) TEM spectrum with EDS elemental mapping of manganese, titanium, oxygen, carbon, and nitrogen (from left to right) of the $LiMn_{1.8}Ti_{0.2}O_4$@N-doped graphene oxide composite.

contained in the hybrid material. The complete Raman spectrum with the deconvolution between 800 and 3000 cm^{-1} is presented in Fig. 2(C). According to the literature reports, the typical Raman spectrum of graphene oxide should present the characteristic bands marked as D, G and 2D. The D and G bands appear at approximately 1350 cm^{-1} and 1520 cm^{-1}, respectively, and are associated with amorphous carbon (D) and graphite carbon (G). The D-band derives from disorder in the sp^2-hybridized carbon, while the G-band is related to the tangential stretching (E_{2g}) mode of graphite [33–35]. The broad-2D band at approximately 2000 cm^{-1} is related to the second-order Raman scattering process [33,36]. The spectra of graphene oxide are characterized by intense D and G bands and a wide 2D band [36]. The Raman results are consistent with those of other reported N-doped graphene oxide materials [37]. The intensity ratio of the D-band to the G-band (I_D/I_G) gives information about the disorder degree of graphene [38]. The I_D/I_G ratio obtained from the deconvoluted D and G bands for the $Li_xMn_{1.8}Ti_{0.2}O_4$@N-doped graphene oxide hybrid material is 0.60, which suggests that there is a low grade of defects and disorders introduced in the graphene oxide material during spinel modification [39].

Additionally, FTIR was employed to identify the functional groups present on the N-doped graphene oxide surface. The FTIR transmittance spectrum of the $Li_xMn_{1.8}Ti_{0.2}O_4$@N-doped graphene oxide sample is presented in Fig. 2(D). First, the narrow peak observed at 1490 cm^{-1} was attributed to the presence of C=C stretching. In addition, C—N stretching was observed at a wavelength of 1380 cm^{-1}, and the typical C=N stretching vibration band at 1322 cm^{-1} also appeared; this peak corresponds to the characteristic bands of nitrogen doping. The bands that appear at 1637 cm^{-1} and 1430 cm^{-1} confirm the occurrence of C=O and C-O-H stretching, respectively. Finally, the typical bands associated with the C—O-C group appear between 1087 and 873 cm^{-1} [40,41]. The FTIR spectrum allowed us to confirm the presence of N-doping into a graphene oxide matrix.

The morphology of the active materials was studied by SEM. The SEM images of the $Li_xMn_{1.8}Ti_{0.2}O_4$ and $Li_xMn_{1.8}Ti_{0.2}O_4$@N-doped graphene oxide samples are shown in Fig. S1(A) and S1(B), respectively, in the supplementary Information. There is a notable difference in the particle shape and size between the samples. The pristine $Li_xMn_{1.8}Ti_{0.2}O_4$ spinel sample presented rounded nanoparticles with comparable sizes between 50 and 80 nm, separated by well-defined boundaries, as shown in Fig. S1(A). The $Li_xMn_{1.8}Ti_{0.2}O_4$@N-doped graphene oxide sample exhibited particle sizes significantly larger than those of the pristine sample, with particle sizes between 300 and 500 nm. This sample presents the typical spinel morphology of octahedron-shaped and composed of {111} surfaces, although slightly less defined compared to the pristine material, as shown in Fig. S1(B). After annealing at elevated temperatures, the particle size increased significantly and favored the growth of a preferential orientation in the crystal, which could significantly affect the electrochemical properties of the active material [42].

Fig. 3 shows TEM images and Fourier image analysis that reveal the distribution of the spinel domain of the $Li_xMn_{1.8}Ti_{0.2}O_4$@N-doped graphene oxide composite. The fast-Fourier transform showing spinel structures with a D-spacing of 0.246 nm (dark blue regions) corresponding to the $LiMn_{1.8}Ti_{0.2}O_4$ spinel (113) plane and the yellow–red regions (*d*-spacing = 0.30 nm) are related to the N-doped graphene oxide matrix; comparatively, the higher transparency areas indicate the spinel structure, and dark areas indicate the stacking nanostructure of several N-doped graphene oxides (Fig. 3(A)). In addition, the high-resolution TEM image of an individual particle shows that the material is formed of octahedrons linked together randomly (Fig. 3(B)). To demonstrate a uniform distribution of elemental Mn, Ti, O, C and N, elemental mapping was obtained, as shown in Fig. 3(C). The EDS mapping reveals that the hybrid material was formed during the post-treatment with 1,10 phenanthroline. As expected, the results confirmed the uniform distribution of N on the graphene oxide matrix and the spinel in the N-graphene oxide matrix.

Table 1
BET surface area of the positive materials.

Material	BET surface Area ($m^2\ g^{-1}$)	Pore Volume Distribution ($cm^3\ g^{-1}$)
$Li_xMn_{1.8}Ti_{0.2}O_4$	3.5	0.007
$Li_xMn_{1.8}Ti_{0.2}O_4$@N-doped graphene oxide	13.5	0.056

This significant size change is also confirmed by Brunauer–Emmett–Teller (BET) analysis, and the BET surface area results are listed in Table 1. Additionally, the nitrogen adsorption/desorption isotherms (type II – IUPAC classification) are provided in Fig. S2 of the Supplementary Information. The BET surface area of the $Li_xMn_{1.8}Ti_{0.2}O_4$ material is significantly lower than that of the $Li_xMn_{1.8}Ti_{0.2}O_4$@N-doped graphene oxide composite. It is easy to associate this increase in the surface area and pore volume to the impregnation of the $Li_xMn_{1.8}Ti_{0.2}O_4$ into the N-doped graphene oxide structure. In addition, the significantly high pore volume distribution for the $Li_xMn_{1.8}Ti_{0.2}O_4$@N-doped graphene oxide material can improve lithium-ion transportation because the electrolyte can impregnate the porous material more easily [28]. Yang et al. [43] reported that metal oxides were uniformly anchored onto the surface of graphene, decreasing the volume expansion/contraction during the cycling process, and that such a network structure can enhance electron conduction [44].

3.2. Electrochemical evaluation

3.2.1. Electrochemical behavior in the LP30 electrolyte

We performed CV experiments to elucidate the electrochemical behavior of the positive electrodes using $Li_xMn_{1.8}Ti_{0.2}O_4$ and $Li_xMn_{1.8}Ti_{0.2}O_4$@N-doped graphene oxide as the active materials and LP30 as the electrolyte. The CV results of the positive electrodes tested in half-cells are presented in Fig. S3. No evident discrepancy in the cyclic voltammograms between the two active materials was observed, indicating similar reaction mechanisms. In the case of the $Li_xMn_{1.8}Ti_{0.2}O_4$ electrode (Fig. S3(A)), the CV displayed two sharp redox peaks at approximately 4.04 V and 3.97 V (peaks I/I*) and 4.14 V and 4.09 V (peaks II/II*), and the CV of the $Li_xMn_{1.8}Ti_{0.2}O_4$@N-doped graphene oxide composite (Fig. S3(B)) also presented two sharp redox peaks at approximately 4.01 V and 3.98 V (peaks I/I*) and 4.14 V and 4.10 V (peaks II/II*). The cyclic voltammograms clearly showed peaks corresponding to redox reactions of the classical spinel $LiMn_2O_4$ between the $LiMn_2O_4$ ($Mn^{4+,3+}$) and λ-MnO_2 (Mn^{4+}) couple during lithium intercalation/deintercalation [14], reaction (1), which can be attributed to topotactic two-phase reversible reactions [45]. The role of titanium in the structure is only to stabilize the spinel structure; therefore, it is electrochemically inert in the potential range under study, 4.6–3.0 V.

$$Li_xMn_{1.8}Ti_{0.2}O_4 \rightleftarrows Mn_{1.8}Ti_{0.2}O_4 + xLi^+ + xe^- \quad (1)$$

Fig. 4 (A and B) shows the galvanostatic charge/discharge profiles corresponding to the cycle numbers (1st, 50th, 70th and 100th) of the pristine $Li_xMn_{1.8}Ti_{0.2}O_4$ and $Li_xMn_{1.8}Ti_{0.2}O_4$@N-doped graphene oxide electrodes, respectively, at a current density of 14.9 mA g^{-1} (0.1 C). Both electrodes showed two charge plateaus at approximately 4.0 V, as was also apparent in the CV results. The $Li_xMn_{1.8}Ti_{0.2}O_4$ electrode presented a discharge specific capacity in the 1st cycle of 54.4 mA h g^{-1} that decayed to 52.2 mA h g^{-1} in the 50th cycle and then to 38.5 mA h g^{-1} in the 70th cycle; however, the specific capacity values decreased over a few cycles, while the $Li_xMn_{1.8}Ti_{0.2}O_4$@N-doped graphene oxide electrode presented an initial capacity of 139.4 mA h g^{-1}, which decayed to 112.1 mA h g^{-1} in the 50th cycle and then to 104 mA h g^{-1} in the 70th cycle, maintaining a capacity retention of 89% higher than that of the pristine material. From the derivation of the GCD curves (Fig. 4(C) and (D)), we obtained the same response as the CV experiments, where the redox peaks associated with the topotactic two-phase reversible

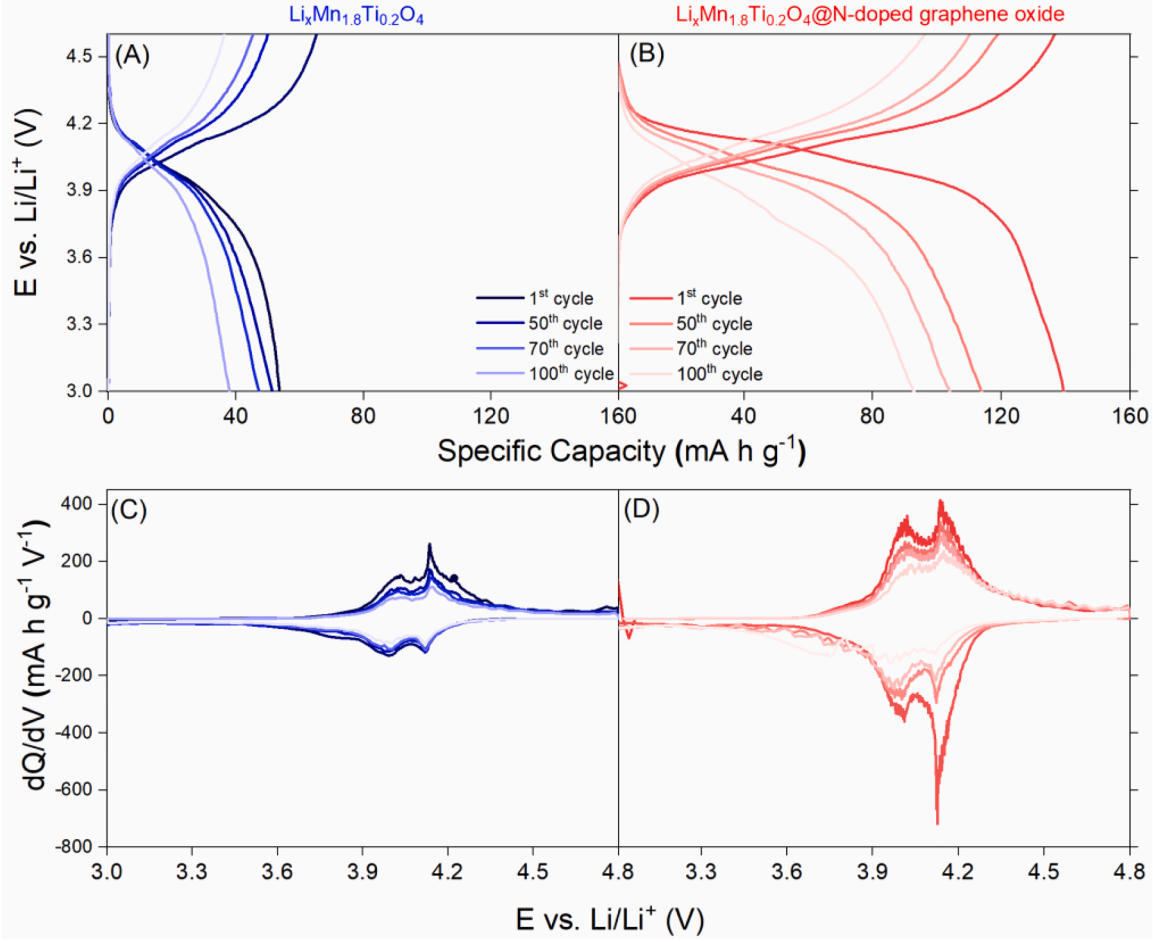

Fig. (A and B) Galvanostatic charge/discharge profiles and (C and D) differential capacity (dq/dV) plots versus voltage of $Li_xMn_{1.8}Ti_{0.2}O_4$ and $Li_xMn_{1.8}Ti_{0.2}O_4$@N-doped graphene composite, respectively. The tests were performed at 14.9 mA g^{-1} (0.1 C-rate) in a voltage range of 3.0–4.6 V in an LP30 electrolyte.

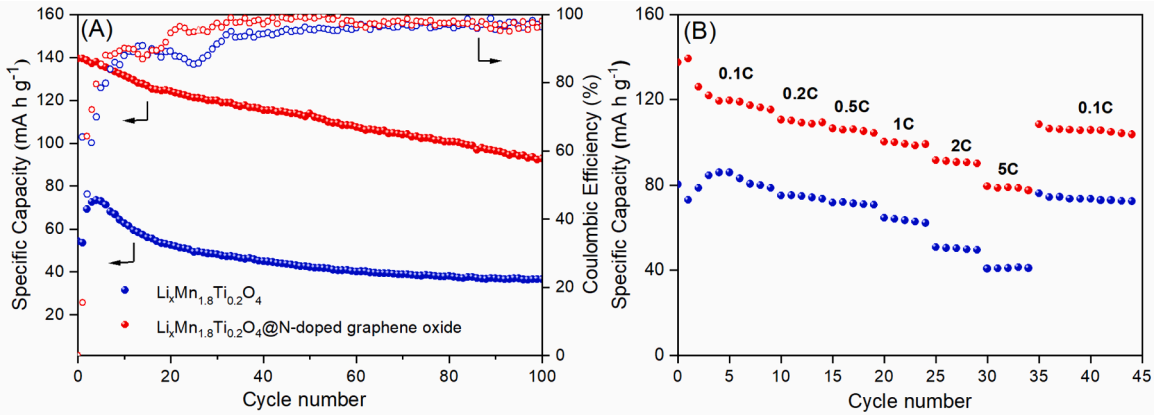

Fig. 5. (A) Cycling performance and coulombic efficiency of $Li_xMn_{1.8}Ti_{0.2}O_4$ and $Li_xMn_{1.8}Ti_{0.2}O_4$@N-doped graphene oxide at 14.9 mA g^{-1} (0.1 C). (B) Rate capability performances at different charge current densities. The tests were performed in a potential range of 4.6 and 3.0 V in an LP30 electrolyte.

reactions are perfectly defined. Furthermore, in the case of the derivate for the $Li_xMn_{1.8}Ti_{0.2}O_4$@N-doepd graphene oxide, we obtained an increase in the charge involved regarding the pure spinel, which is associated with an enhancement in the electrical and ionic conductivity of the material due to the N-doped graphene oxide sheets inserted into the spinel, as demonstrated above.

The cycling stability and the corresponding coulombic efficiency of the $Li_xMn_{1.8}Ti_{0.2}O_4$ and $Li_xMn_{1.8}Ti_{0.2}O_4$@N-doped graphene oxide electrodes in the potential range of 4.6 – 3.0 V at 0.1 C (1 C = 149 mA g^{-1}) are presented in Fig. 5(A). The $Li_xMn_{1.8}Ti_{0.2}O_4$@N-doped graphene oxide electrode presented a better cycling stability than the pure $Li_xMn_{1.8}Ti_{0.2}O_4$ electrode. The initial discharge capacity of the $Li_xMn_{1.8}Ti_{0.2}O_4$@N-doped graphene oxide electrode was 139 mA h g^{-1}, and it exhibited 81% charge retention after 70 cycles, while the $Li_xMn_{1.8}Ti_{0.2}O_4$ electrode presented an initial discharge capacity of 73 mA h g^{-1}, which is lower than that of the composite electrode. In

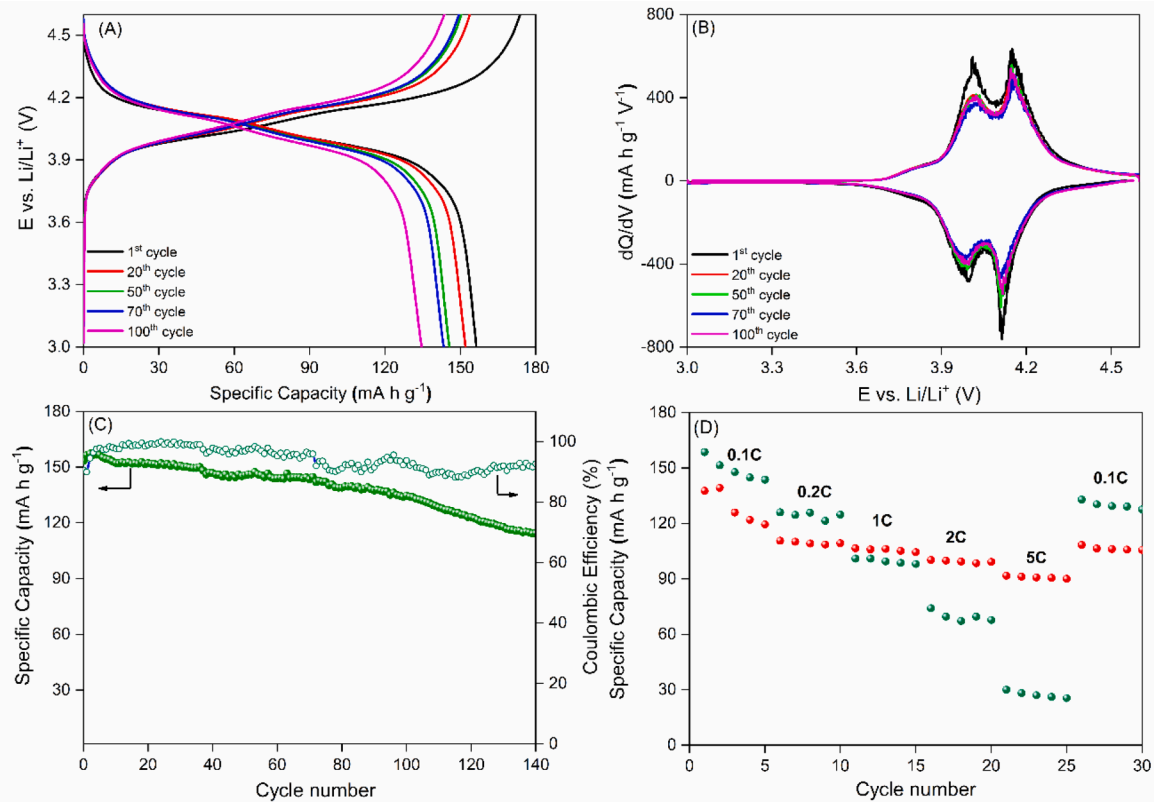

Fig. 6. (A) Galvanostatic charge/discharge profiles. (B) Differential capacity (dq/dV) plots versus voltage of the $Li_xMn_{1.8}Ti_{0.2}O_4$@N-doped graphene oxide composite corresponding to cycle numbers 1st, 50th, 70th and 100th. (C) Cycling performance and coulombic efficiency vs. cycle number. The tests were performed in a potential range of 3.0–4.6 V in a 1 mol L^{-1} LiTFSI/[($Pyr_{1,4}$)(TFSI)] electrolyte. (D) Rate capability performances at different discharge current densities of the $Li_xMn_{1.8}Ti_{0.2}O_4$@N-doped graphene oxide composite in 1 mol L^{-1} LP30 (red) and 1 mol L^{-1} LiTFSI/[($Pyr_{1,4}$)(TFSI)] (green) electrolytes at 25 °C.

addition, the coulombic efficiencies for both positive electrodes were maintained near 96% during the 70 cycles performed. Fig. 5(B) shows the rate capability performance of the $Li_xMn_{1.8}Ti_{0.2}O_4$ and $Li_xMn_{1.8}Ti_{0.2}O_4$@N-doped graphene oxide electrodes. The $Li_xMn_{1.8}Ti_{0.2}O_4$@N-doped graphene oxide electrode exhibits a much better rate capability performance than the pristine spinel electrode. The discharge capacity decreased gradually as the current rate increased from 0.1 C to 5 C, and in all cases, the charge current was 0.1 C. In particular, the $Li_xMn_{1.8}Ti_{0.2}O_4$@N-doped graphene oxide electrode can deliver considerably high specific capacity values on discharges of 139, 109, 106, 99, 91 and 79 mA h g^{-1} at current discharges of 0.1 C, 0.2 C, 0.5 C, 1 C, 2 C and 5 C, respectively; these values are higher than those exhibited by the pristine $Li_xMn_{1.8}Ti_{0.2}O_4$ electrode, which were 86, 75, 71, 63, 50 and 41 mA h g^{-1}. In addition, at a 2 C discharge rate, the $Li_xMn_{1.8}Ti_{0.2}O_4$@N-doped graphene oxide electrode presented a specific capacity of 91 mA h g^{-1}, while the capacity of the $Li_xMn_{1.8}Ti_{0.2}O_4$ electrode was 50 mA h g^{-1}. The stable reversible capacity of $Li_xMn_{1.8}Ti_{0.2}O_4$@N-doped graphene oxide reverted to 108 mA h g^{-1} when the current returned to 0.1 C. The novel composite electrode exhibited a distinctly superior rate capacity performance, which may be related to the good electron conductivity of the N-doped graphene sheets and to the additional morphology changes conferred by the composite material synthesis.

3.2.2. *Electrochemical performance of the $Li_xMn_{1.8}Ti_{0.2}O_4$@N-doped graphene oxide electrode tested in LP30 and IL-based electrolytes*

As discussed in the introduction, ILs may improve the electrochemical and thermal stability of LIB systems constituted by high capacity/high voltage positive electrode materials when used as electrolytes. Elevated temperature also results in poor battery performance, which accelerates the oxidative degradation of electrolytes. Degradation of the carbonate electrolyte produces a large number of byproducts, which in turn affects the coulombic efficiency of the battery and rapidly decays the cycle life [46]. Thus, there is a possibility of IL application in high potential Li-ion batteries and, in particular, their behavior with high voltage positive materials should be studied. Here, we already showed the compatibility of our hybrid material on an IL-based electrolyte. Fig. 6 shows the electrochemical performance of the $Li_xMn_{1.8}Ti_{0.2}O_4$@N-doped graphene oxide composite material tested in a 1 mol L^{-1} LiTFSI/[($Pyr_{1,4}$)(TFSI)] electrolyte. Fig. 6(A) shows the GCD curves of the active material performed at 14.9 mA g^{-1} (0.1 C) and at 25 °C. A specific capacity of 135 mA h g^{-1} was obtained in cycle number 100, and this capacity is comparable with the values obtained in the LP30 electrolyte. Furthermore, the differential capacity of each GCD curve showed two characteristic peaks (see Fig. 6(B)) corresponding to the topotactic two-phase reversible reactions [45] already observed in the materials tested in the LP30 electrolyte. In addition, as shown in Fig. 6(C), an enhancement of the cycling life of the $Li_xMn_{1.8}Ti_{0.2}O_4$@N-doped graphene oxide electrode was observed, with a specific capacity of approximately 120 mA h g^{-1} in cycle number 140. The rate capability of the $Li_xMn_{1.8}Ti_{0.2}O_4$@N-doped graphene oxide electrode in LP30 and the IL-based electrolyte was also investigated. Fig. 6 (D) and Fig. S4 compare the rate capability performances at temperatures of 25 °C and 40 °C, respectively. At 25 °C, the performance of both cells was comparable by the 15th cycle at 1 C, reaching almost the same capacity (100 mA h g^{-1}). When the rate was further increased to 2 C and 5 C, the capacity of the cell with the IL-based electrolyte dropped to values lower than 70 mA h g^{-1}, while for the cell with LP30, the values were greater than 90 mA h g^{-1}. In contrast, at 40 °C, the discharge capacity of the cell with the IL-based electrolyte had an improved rate capability, delivering 115 mA h g^{-1} and 104 mA h g^{-1} at 0.1 C and 2 C, respectively. The same behavior was observed in the cell with LP30, where the rate capability was 119 mA h g^{-1} and 106 mA h g^{-1} at 0.1 C

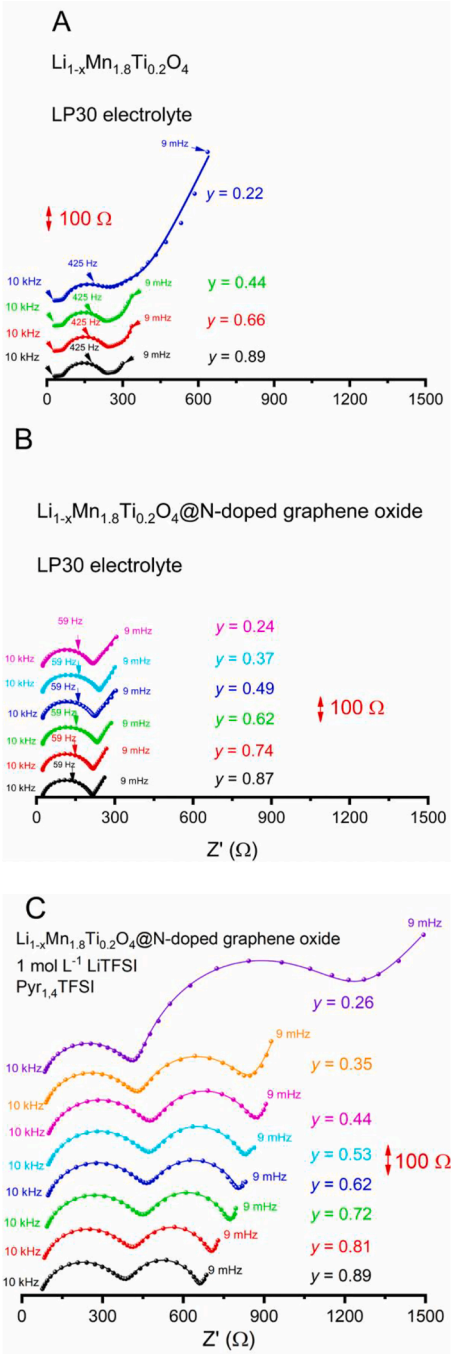

Fig. 7. Nyquist plots of EIS data recorded at different states of charge in the LP30 electrolyte of (A) $Li_xMn_{1.8}Ti_{0.2}O_4$ and (B) $Li_xMn_{1.8}Ti_{0.2}O_4$@N-doped graphene oxide. (C) $Li_xMn_{1.8}Ti_{0.2}O_4$@N-doped graphene oxide in an IL-based electrolyte.

and 2 C, respectively. It is important to mention that at 40 °C, the cell with the 1 mol L^{-1} LiTFSI/[($Pyr_{1,4}$)(TFSI)] electrolyte had a remarkably high and stable rate performance because the physiochemical properties, specially the ion conductivity, of the IL-based electrolyte improved strongly with increasing temperature. Thus, at 40 °C, lithium extraction/insertion was facilitated by an increase in temperature [47,48].

A more detailed analysis of the electrochemical performance of the active materials tested in both LP30 and IL-based electrolytes was performed by EIS at different states of charge and discharge. Each EIS experiment was performed in a three-electrode cell as follows: a fresh electrode, which was stabilized by performing 30 discharge/charge cycles at a constant current density of C/10, was used. Afterward, the completely delithiated electrode was discharged at C/10 with a different applied cutoff of discharge. When the cutoff was achieved, the circuit was opened for 30 min, and the measured potential was applied for 30 min. Finally, the EIS experiment was carried out at the registered OCP. Fig. S5 shows the E vs. t curves of the experiment (with $Li_xMn_{1.8}Ti_{0.2}O_4$@N-doped graphene oxide as an example), representing how the above sequence was performed. Fig. 7 shows the Nyquist plots of the EIS experiments at different amounts of lithium (x) in $Li_xMn_{1.8}Ti_{0.2}O_4$-based electrodes for the three conditions under analysis, i.e., $Li_xMn_{1.8}Ti_{0.2}O_4$, $Li_xMn_{1.8}Ti_{0.2}O_4$@N-doped graphene oxide, both in the LP30 electrolyte and $Li_xMn_{1.8}Ti_{0.2}O_4$@N-doped graphene oxide in the IL-based electrolyte. All experiments were performed at 25 °C.

The overall impedance resistances of pure $Li_xMn_{1.8}Ti_{0.2}O_4$ were higher than those of $Li_xMn_{1.8}Ti_{0.2}O_4$@N-doped graphene oxide (comparing Fig. 7(A) and (B)). This decrease in all resistances is associated with the graphene oxide network, where $Li_xMn_{1.8}Ti_{0.2}O_4$ was incorporated, improving the conductivity between the particles. Furthermore, the overall impedance resistances of the $Li_xMn_{1.8}Ti_{0.2}O_4$@N-doped graphene oxide in the IL-based electrolyte were even higher than those in the organic electrolyte (Fig. 7(C)). In this case, the two semicircles are perfectly separated, and the diffusion contribution is completely diminished; we associated this phenomenon with poor Li-ion diffusion in the IL-medium in the frequency range that we performed the EIS experiments. Additionally, in all cases, the overall resistance decreased as the amount of intercalated lithium was increased, which is attributed to the formation of a more conductive material (by the presence of Mn^{3+} in the spinel) [45], as can be observed in Eq. (1). In Fig. S6, we present the Nyquist plots of the discharge of pure $Li_xMn_{1.8}Ti_{0.2}O_4$, $Li_xMn_{1.8}Ti_{0.2}O_4$@N-doped graphene oxide, both in the LP30 electrolyte, and $Li_xMn_{1.8}Ti_{0.2}O_4$@N-doped graphene oxide in the IL-based electrolyte.

By fitting the measured data with an electrochemical equivalent circuit (EEC), we obtained detailed information about the electrochemical processes. The EEC used to fit the experimental EIS data for the $Li_xMn_{1.8}Ti_{0.2}O_4$ and $Li_xMn_{1.8}Ti_{0.2}O_4$@N-doped graphene oxide electrodes is represented in Fig. S7. The EEC consisted of the electrolyte resistance (R_{EL}) in a series with a parallel arrangement between resistance and a constant phase element (CPE), which was associated with the cathodic electrolyte interface (CEI) layer formed on the positive electrode surface ($R_{CEI}|CPE_{CEI}$). This is linked to a second parallel arrangement of a polarization resistance (R_p) and a CPE of the double layer (CPE_{dl}) representing the charge transfer reaction of the active material and a T diffusion element with a constant $\alpha < 0.5$ in series with the resistance ($R_pT|CPE_{dl}$). R_{EL} can be directly obtained from the impedance spectra and equals zero when crossing the real Z axis at high frequencies. $R_{CEI}|CPE_{CEI}$ and $R_pT|CPE_{dl}$ are observed as a depressed capacitive loop in the middle-frequency region, and the respective time constants appear coupled when the electrodes are tested in the LP30 electrolyte. The diffusion process is reflected in the lower-frequency region.

In Fig. S8, we show the representation of the phase angle vs. log (frequency) (Bode plot), which easily reflects the different time constants. For instance, in the Nyquist plots of the $Li_xMn_{1.8}Ti_{0.2}O_4$@N-doped graphene oxide in LP30, there seems to be one time constant; however, in the Bode plot of the phase angle, two overlapping time constants are clearly observed.

The different resistance values were obtained by fitting the EIS spectra and were plotted as a function of *x* of lithium (for both lithiation and delithiation processes) for pure $Li_xMn_{1.8}Ti_{0.2}O_4$ and $Li_xMn_{1.8}Ti_{0.2}O_4$@N-doped graphene oxide in LP30, Fig. 8(A) and (C), respectively. In the Supplementary Information the Table S1, Table S2 and Table S3 inform the resistance and capacitance values for pure $Li_xMn_{1.8}Ti_{0.2}O_4$ and $Li_xMn_{1.8}Ti_{0.2}O_4$@N-doped graphene oxide both in LP30 and $Li_xMn_{1.8}Ti_{0.2}O_4$@N-doped graphene oxide in IL-based electrolyte, respectively. The resistance values of $Li_xMn_{1.8}Ti_{0.2}O_4$@N-doped

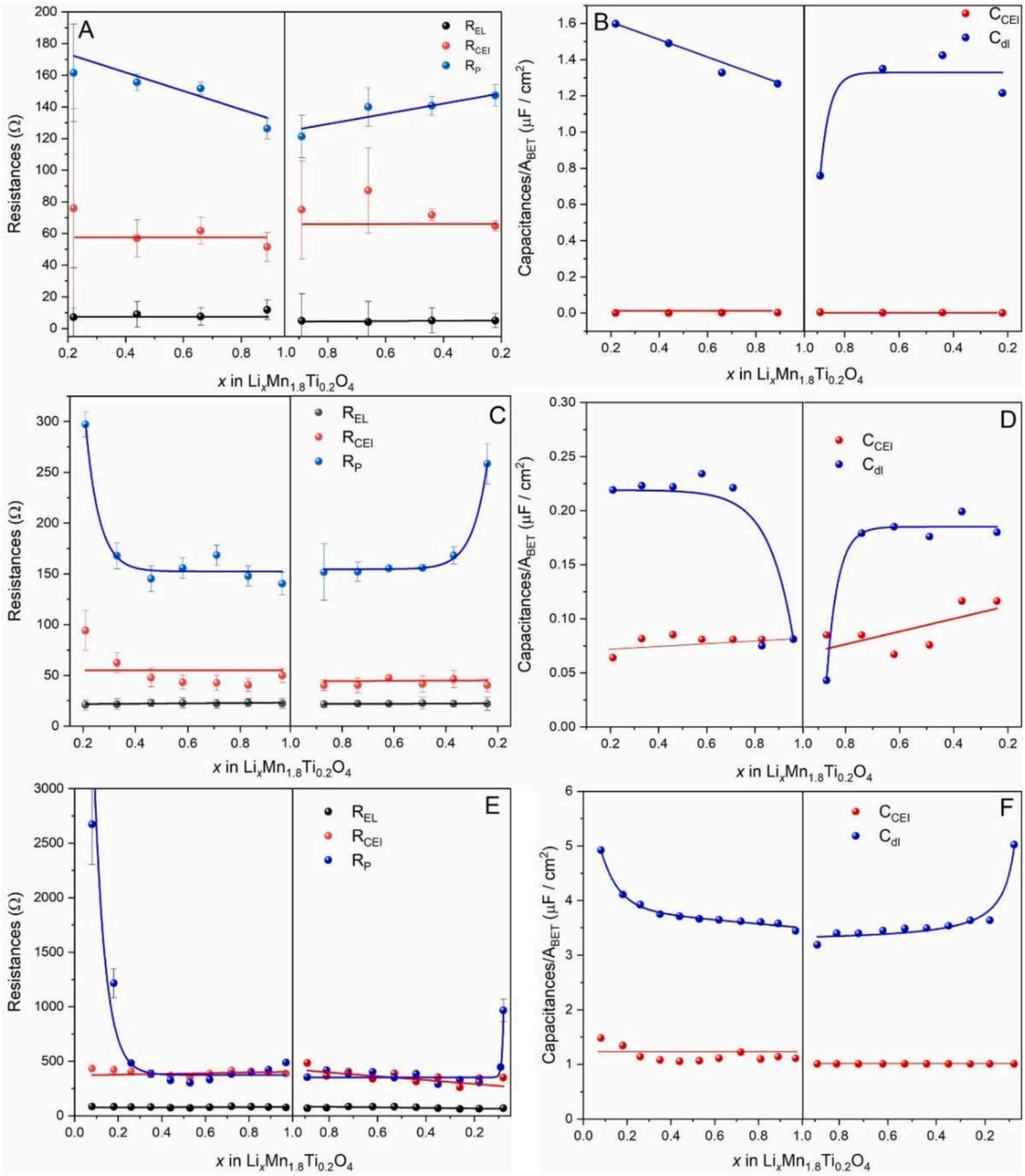

Fig. 8. Resistances and capacitances obtained from the fitting of the EIS spectra at different states of lithiation and delithiation in the LP30 electrolyte for (A) and (B) pure $Li_xMn_{1.8}Ti_{0.2}O_4$ (C) and (D) $Li_xMn_{1.8}Ti_{0.2}O_4$@N-doped graphene oxide. (E) and (F) represent $Li_xMn_{1.8}Ti_{0.2}O_4$@N-doped graphene oxide in an IL-based electrolyte. Color code: blue symbols correspond to the resistance of polarization, red symbols to the resistance of CEI and black symbols to the resistance of the electrolyte. All the lines in the figure are a guide.

graphene oxide tested in the IL-based electrolyte are shown in Fig. 8(E). The R_P, R_{CEI} and R_{EL} values are lower for $Li_xMn_{1.8}Ti_{0.2}O_4$@N-doped graphene oxide than those exhibited by the pure $Li_xMn_{1.8}Ti_{0.2}O_4$ active material, suggesting the enhancement in the electrical conductivity by the incorporation of the N-doped graphene oxide. As expected, in the three cases, the R_{EL} and R_{CEI} values were practically unchanged throughout the lithiation and delithiation processes. In contrast, because R_P describes the electrical properties of the material, as the amount of lithium is increased (i.e., more conductive spinel in the presence of Mn^{3+}), the R_P values decrease.

In addition, we determined the capacitances (C) using the CPE constant values (Q and α) obtained from the fittings. The capacitance values associated with the CEI and the double layer as a function of the lithiation state are plotted in Fig. 8(B), (D) and (F) for $Li_xMn_{1.8}Ti_{0.2}O_4$ in LP30, $Li_xMn_{1.8}Ti_{0.2}O_4$@N-doped graphene oxide in LP30 and $Li_xMn_{1.8}Ti_{0.2}O_4$@N-doped graphene oxide in the IL-based electrolyte, respectively. We used the Brug equation to calculate the capacitances [49]:

$$C = \left[\frac{Q}{\left(R^{-1} + Rel^{-1}\right)^{(1-\alpha)}}\right]^{\frac{1}{\alpha}} \quad (2)$$

The capacitance values of the CEI in the three cases did not change with the state of lithiation of the materials. In contrast, the capacitances of the double layer decreased as the amount of lithium was increased and followed the same trend as the R_P. However, the capacitance values

were lower for $Li_xMn_{1.8}Ti_{0.2}O_4$@N-doped graphene oxide than those exhibited by pure $Li_xMn_{1.8}Ti_{0.2}O_4$. Therefore, throughout the lithiation process (as a consequence of the reduction of Mn^{4+}, as described in the section on the CV experiments), the spinel became more conductive, making the double layer thinner. Additionally, Because the capacitances are normalized by the BET area of the samples, it is possible to analyze the CEI thickness formed in both electrolytes, which is inversely proportional to the capacitance value (where the dielectric constants are approximately equal). The thickness of the CEI formed in the IL was lower than that formed in the LP30 electrolyte; however, due to the resistance of both CEIs (R_{CEI}), the CEI formed in organic solvent was probably more porous and conductive and more permeable to lithium ions.

We also obtained the time constant (τ) as the amount of lithium was changed, and we compared the pristine and hybrid materials in the LP30 electrolyte (Fig. S9). The most important difference is that the hybrid material required less time than the pristine material, suggesting faster charge transfer. Furthermore, the trends in the variation of τ as the amount of lithium was changed were the same as those of the Rp of both materials in LP30.

From the imaginary resistance (diffusion part) of the Nyquist plot versus the inverse square root of angular frequency ($\omega^{-1/2}$), we obtained the diffusion coefficient of lithium-ion (D_{Li+}) for the more discharged state (more lithiated spinel), according to the following equation [50].

$$D_{Li+} = \frac{R^2T^2}{2A^2n^4F^4C^2\sigma^2} \quad (3)$$

Where R is the gas constant, T is the absolute temperature, F is the Faraday constant (96,486 C mol^{-1}), A is the geometric surface area, n is the number of electrons exchanged and C is the lithium-ion concentration, and σ is the slope of the imaginary resistance (Z_{im}) vs. the inverse of the angular frequency (ω^{-1}). We obtained values of D_{Li+} of 1.77×10^{-10} cm^2 s^{-1} and 6.37×10^{-11} cm^2 s^{-1} for $Li_xMn_{1.8}Ti_{0.2}O_4$@N-doped graphene oxide and pure $Li_xMn_{1.8}Ti_{0.2}O_4$, respectively. Not only the obtained D_{Li+} values are characteristic of this kind of system, where lithium ions are intercalated in a solid structure, but also it was obtained a higher D_{Li+} for the hybrid material, which corresponds to the material with better ionic conductivity [51,52], as it was described before. Finally, the electrical conductivity of the materials was obtained using the current vs. potential (i vs. E) measurements in a two-cell terminal. The slope of the resulting i vs. E plots were used to calculate the electrical conductivity considering the materials geometric distribution, according to the following equation [53].

$$\sigma_{i,e} = \left(\frac{1}{R_{i,e}}\right)\left(\frac{L}{A}\right) \quad (4)$$

Where $\sigma_{i,e}$ is the electrical conductivity, $R_{i,e}$ is the electrical resistance, L is the thickness of the active materials, and A is the geometric area of the electrode. The electrical conductivity values obtained for pure $Li_xMn_{1.8}Ti_{0.2}O_4$ and $Li_xMn_{1.8}Ti_{0.2}O_4$@N-doped graphene oxide were 1.25 μS cm^{-1} and 4.77 μS cm^{-1}, respectively. The hybrid material $Li_xMn_{1.8}Ti_{0.2}O_4$@N-doped graphene oxide showed values of electrical conductivity significantly larger than the $Li_xMn_{1.8}Ti_{0.2}O_4$ pure spinel, thanks to the incorporation of conductive carbon substrate. As it has been reported from other studies, the electrical conductivity values of manganese oxide are between 1.0 and 10 μS cm^{-1} [54]. The absolute conductivity values obtained in the current work are comparable to literature reports.

XPS measurements were performed to investigate the formation of the CEI on a carbon sheet electrode surface cycled using the LP30 and LiTFSI/[($Pyr_{1,4}$)(TFSI)] electrolytes. The survey spectra obtained after the first discharge demonstrate that the CEI formed on the carbon sheet surface differs in composition in each electrolyte. The carbon sheet cycled with LP30 and the Li electrode (called C/LP30) showed F 1 s, O 1 s, C 1 s and P 2p spectra (Fig. S10(A)), while the electrode cycled with the IL (called C/IL-based) showed F 1 s, O 1 s, C 1 s, N 1 s and S 2p spectra (Fig. S10(B)) related to CEI formation on each electrode surface.

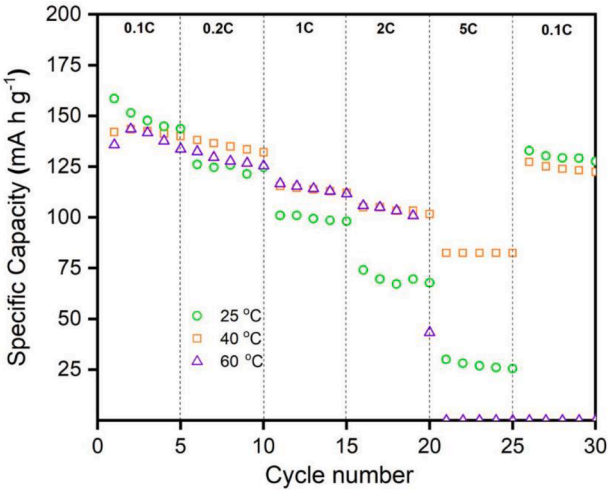

Fig. 9. Rate capability performance at different temperatures and charge current densities of the $Li_xMn_{1.8}Ti_{0.2}O_4$@N-doped graphene oxide composite. The tests were performed in a voltage range of 3.0–4.6 V in 1 mol L^{-1} LiTFSI/[($Pyr_{1,4}$)(TFSI)] electrolyte.

For the C/LP30 surface, the photoelectron emission bands in the 532 and 533.6 eV binding energy ranges are attributed to C−O and C=O, respectively, which are dominating species in the O 1 s spectrum (Fig. S10 (C)), indicating that the carbonate solvent (EC:DMC) decomposed during the process, participating in CEI formation [55,56]. The peak of fluorine indicates two bonds [7], the C-F bond at ~688 eV and the P-F bond at 686.5 eV. This spectrum is attributed to the degradation of the salt [55]. In addition, a weak signal at ~135.1 eV in the P 2p spectrum (Fig. S10 (C)) is attributed to P–Li species, which implies the participation of $LiPF_6$ salt in CEI layer formation [47].

In contrast, the C/IL-based surface formed in ($Pyr_{1,4}$)(TFSI) electrolyte presented in Fig. S10(D) shows the O 1 s photoelectron emission band. The binding energy of 531.5 eV is attributed to C − O bonds, and the 533.0 eV emission band corresponds to C = O bonds [7]. Furthermore, in the IL-based electrolyte, it shows a significant number of SO_2 moieties in the ~532.9 eV binding energy, derived from the decomposition of FSI^- anions [7,57]. Moreover, the deconvolution of the S 2p spectrum confirms the presence of the SO_2 group from FSI breakdown. The 169.3 and 170.5 eV binding energies are attributed to $2p_{3/2}$ and $2p_{1/2}$, respectively, indicating that the electrolyte participates in the formation of the CEI layer. The S 2p spectrum clearly shows the presence of SO_2 [58]. Similarly, the N 1 s photoelectron spectrum is shown in Fig. S10 (B). The spectrum of two well-defined peaks at ~398.9 eV and ~401.8 eV occur, which are assigned to the N–S bond in the LiTFSI electrolyte, confirming that the $TFSI^-$ anion contributes to the formation [59,60]. The appearance of LiF in the F 1 s (~685.2 eV) and C-F (~687.6 eV) spectra suggests the decomposition of the LiTFSI on the carbon sheet electrode surface [7].

When we used $Li_xMn_{1.8}Ti_{0.2}O_4$@N-doped graphene oxide in both electrolytes, the first electrochemical cycle led to the formation of a CEI, which is the result of the deterioration of the electrolyte and the salt due to surface reactions.

Finally, we performed rate capability experiments using the $Li_xMn_{1.8}Ti_{0.2}O_4$@N-doped graphene oxide electrode in the IL electrolyte at different temperatures. We found that there was a clear dependence since temperature greatly influenced the physiochemical properties (viscosity and conductivity) of the IL-based electrolyte. The rate capability profiles of the $Li_xMn_{1.8}Ti_{0.2}O_4$@N-doped graphene oxide electrode were evaluated at 25 °C, 40 °C and 60 °C (Fig. 9). At 25 °C, the $Li_xMn_{1.8}Ti_{0.2}O_4$@N-doped graphene oxide electrode exhibited moderate

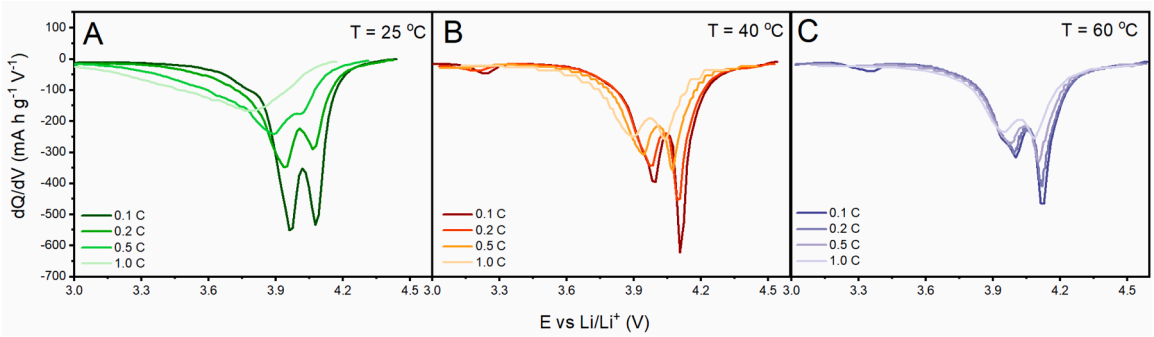

Fig. 10. Differential capacity (dq/dV) plots versus voltage of the $Li_xMn_{1.8}Ti_{0.2}O_4$@N-doped graphene oxide composite performed at different currents (C-Rate). The tests were performed in a voltage range of 3.0–4.6 V in 1 mol L^{-1} LiTFSI/[($Pyr_{1,4}$)(TFSI)] electrolyte at 25 °C (A), 40 °C(B) and 60 °C (C).

discharge capacities of 116 and 100 mA h g^{-1} at high C-rates of 0.5 C and 1 C, respectively. The discharge capacity values of the $Li_xMn_{1.8}Ti_{0.2}O_4$@N-doped graphene oxide electrode further increased to 129 mA h g^{-1} and 117 mA h g^{-1} at rates of 0.5 C and 1 C, respectively, when cycling at 40 °C. This response shows an optimal temperature where the viscosity and conductivity of the IL allows a favored diffusion of lithium ions. However, the discharge capacities decreased to 125 mA h g^{-1} and 116 mA h g^{-1} at 0.5 C and 1 C, respectively, when cycling at 60 °C. Moreover, the rapid capacity decayed at rates of 5 C and 10 C due to the thermal stability of the IL at high temperatures.

In Fig. 10, we show the derivative of charge vs. potential (dQ/dV vs. E) profiles corresponding to the fifth cycle at each rate performed at different temperatures. This representation offers an approach to estimating the fraction of charge assigned to each redox couple and how this fraction changes at different rates. Similar to that of the $Li_xMn_{1.8}Ti_{0.2}O_4$@N-doped graphene oxide electrode in the organic electrolyte, two potential plateaus were observed for each discharge curve, showing the double steps of lithium extraction/insertion from/into $Li_xMn_{1.8}Ti_{0.2}O_4$@N-doped graphene oxide. When the electrode was cycled at 25 °C and a high rate, the fraction of charge assigned to each redox couple decreased with the cycles. Nevertheless, when the rate capability experiments were performed at 40 °C and 60 °C using the $Li_xMn_{1.8}Ti_{0.2}O_4$@N-doped graphene oxide electrodes, the charge involved in both processes remained the same at all the applied rates. This result confirms that not only the properties of the IL but also the kinetic properties of the electrochemical reactions were favored at increased temperatures for this application.

4. Conclusions

In summary, we first enhanced the electrochemical response of $Li_xMn_{1.8}Ti_{0.2}O_4$ through by supporting it on porous N-doped graphene oxide in LP30 as an electrolyte. Using XRD, Raman spectroscopy and FTIR spectroscopy, we determined that the $Li_xMn_{1.8}Ti_{0.2}O_4$ and $Li_xMn_{1.8}Ti_{0.2}O_4$@N-doped graphene oxide materials were successfully synthesized. From the fast-Fourier transform of the TEM images, we obtained the typical spinel and carbonaceous structures and *d*-spaces related to the corresponding phases of $Li_xMn_{1.8}Ti_{0.2}O_4$@N-doped graphene oxide. Furthermore, EDS mapping showed a uniform distribution of N on the carbon matrix and spinel into the N-graphene oxide matrix. Additionally, the BET surface area of the hybrid material was increased 4 times compared with that of the pristine material due to the impregnation of the spinel particles on a porous carbonaceous matrix.

Lithium-ion storage properties were determined through numerous electrochemical techniques. First, using LP30 as the electrolyte, the CV experiments and the differential capacity of the GCD curves showed the typical peaks corresponding to redox reactions of the classical spinel $LiMn_2O_4$ couple during Li intercalation/deintercalation, which is attributed to topotactic two-phase reversible reactions. We obtained an enhancement in the charge involved in the case of the hybrid material due to the improvement in the conductivity of the hybrid material. In terms of cyclability, we obtained more than 80% capacity retention over 70 cycles. Since one of the abilities of this material is the high potential range, we employed IL-based electrolytes. We performed complete characterization using EIS at different states of charge and discharge comparing pristine and hybrid materials on both kinds of electrolytes. From the different electrical parameters obtained, such as resistances and capacitances, we determined that the hybrid material enhanced the electrical conductivity, reflecting a better charge transfer process. We also determined that on both electrolytes, the CEI was formed (characterized by XPS) and was thicker when we used LP30 and more conductive than when we used IL (as shown by the values of the resistances associated with the CEI).

Finally, a long cycle performed at 25 °C and a rate capability response at 40 °C, both at 0.5 C using 1 mol L^{-1} LiTFSI/[($Pyr_{1,4}$)(TFSI)] as the electrolyte, showed superior specific capacities of 116 mA h g^{-1} and 129 mA h g^{-1}, respectively. Therefore, the electrochemical properties of the $Li_xMn_{1.8}Ti_{0.2}O_4$@N-doped graphene oxide electrode were strongly influenced by the variation in temperature and consequent changes in the physicochemical properties of the IL-based electrolyte.

Data availability statement

The authors declare that data of current manuscript are available on reasonable request from the interested.

CRediT authorship contribution statement

Nerly Mosquera: Conceptualization, Investigation, Methodology, Writing – review & editing. **Susana Chauque:** Conceptualization, Investigation, Methodology, Writing – review & editing. **Roberto M. Torresi:** Conceptualization, Methodology, Project administration, Funding acquisition, Supervision, Writing – review & editing. **Jorge A. Calderón:** Conceptualization, Methodology, Project administration, Funding acquisition, Supervision, Writing – review & editing.

Declaration of Competing Interest

The authors declare that they have no known competing financial interests or personal relationships that could have appeared to influence the work reported in this paper.

Data availability

Data will be made available on request.

Acknowledgments

This work was supported by the CNPq, CAPES and FAPESP (2015/

26308-7, 2020/03543-9 and 2021/00675-4), and Comité para el Desarrollo de la Investigación, CODI – UdeA (project 151951). SC wish to thank FAPESP for financial support (2018/11320-0). N.M. wish to thank CIERCLIMA - UTCH (project BPIN: 2020000100330) and "Ministerio de Ciencia Tecnología e Innovación - Minciencias" for the PhD scholarship 785 of 2017.

Supplementary materials

Supplementary material associated with this article can be found, in the online version, at doi:10.1016/j.electacta.2023.142210.

References

[1] J.-H. Shim, J. Lee, S.Y. Han, S. Lee, Synergistic effects of coating and doping for lithium-ion battery cathode materials: synthesis and characterization of lithium titanate-coated $LiCoO_2$ with Mg doping, Electrochim. Acta 186 (2015) 201–208.
[2] T.F. Yi, T.T. Wei, Y. Li, Y.B. He, Z.B. Wang, Efforts on enhancing the Li-ion diffusion coefficient and electronic conductivity of titanate-based anode materials for advanced Li-ion batteries, Energy Storage Mater. 26 (2020) 165–197.
[3] J. Kalhoff, G. Eshetu, D. Bresser, Safer electrolytes for lithium-ion batteries: state of the art and perspectives, (2015) 2154–2175.
[4] E. Fan, L. Li, Z. Wang, J. Lin, Y. Huang, Y. Yao, R. Chen, F. Wu, Sustainable Recycling Technology for Li-Ion Batteries and Beyond: challenges and Future Prospects, Chem. Rev. 120 (2020) 7020–7063.
[5] G. Pagot, F. Bertasi, G. Nawn, E. Negro, G. Carraro, D. Barreca, C. Maccato, S. Polizzi, V. di Noto, High-Performance olivine for lithium batteries: effects of Ni/Co Doping on the Properties OF $LiFe_\alpha Ni_\beta Co_\gamma PO_4$ Cathodes, Adv. Funct. Mater. 25 (2015) 4032–4037.
[6] J. Zheng, S. Myeong, W. Cho, P. Yan, J. Xiao, C. Wang, J. Cho, J.G. Zhang, Li- and Mn-rich cathode materials: challenges to commercialization, Adv. Energy Mater. 7 (2017).
[7] H.J. Lee, Z. Brown, Y. Zhao, J. Fawdon, W. Song, J.H. Lee, J. Ihli, Ordered LiNi0.5Mn1.5O4 cathode in Bis(fluorosulfonyl)imide-based ionic liquid electrolyte: importance of the cathode−electrolyte interphase, Chem. Lett. 33 (2021) 1238–1248.
[8] N. Hung, V. Dao, H.N. Van, L. Thanh, Spinel-layered Li_2MnTiO_{4+z} nanofibers as cathode materials for Li-ion batteries, Solid State Sci. 103 (2020), 106178.
[9] C.Y. Ouyang, S.Q. Shi, M.S. Lei, Jahn-Teller distortion and electronic structure of $LiMn_2O_4$, J. Alloy. Compd. 474 (2009) 370–374.
[10] L.M. Uribe-Grajales, F.A. Vásquez-Arroyave, J.E. Thomas, J.A. Calderón-Gutiérrez, Evaluation of the effect of the synthesis method on the performance of manganese spinel as cathode material in lithium-ion batteries, Rev. Facult. Ing. (2018) 41–49.
[11] N.H. Vu, P. Arunkumar, S. Won, H.J. Kim, S. Unithrattil, Effects of excess Li on the structure and electrochemical performance of $Li_{1+z}MnTiO_{4+\delta}$ cathode for Li-ion batteries, Electrochim. Acta 225 (2017) 458–466.
[12] A.M. Amigues, J. Electrochem, A. Soc, A.M. Amigues, H.F.J. Glass, S.E. Dutton, LiMnTiO4 with the Na0.44MnO2 structure as a positive electrode for lithium-ion batteries, (2016) 3–8.
[13] T. Kesavan, C. Senthil, M. Sasidharan, Solvothermally synthesized Ti-rich $LiMnTiO_4$ as cathode material for high Li storage, J. Mater. Sci. 53 (2018) 4406–4416.
[14] N. Mosquera, F. Bedoya-Lora, V. Vásquez, F. Vásquez, J. Calderón, Capacity fading of high specific capacity spinel $Li_xMn_{2-y}Ti_yO_4$ as cathode material for Li-ion batteries, J. Appl. Electrochem. 51 (2021) 1419–1435.
[15] Jianliang cheng, Xinhai Li, Zhenjiang He, H. Guo, W. Peng, Significant improved electrochemical performance of layered $Li_{1.2}Mn_{0.54}Co_{0.13}Ni_{0.13}O_2$ via graphene s. pdf, Mater. Technol. Adv. Perfor. Mater. 31 (2016) 658–665.
[16] A.H. Marincaş, P. Ilea, Enhancing lithium manganese oxide electrochemical behavior by doping and surface modifications, Coatings 11 (2021).
[17] X. Zhang, M. Yang, X. Zhao, Y. Wang, M. Wang, The spinel phase $LiMnTiO_4$ as a potential cathode for rechargeable lithium-ion batteries, J. Mater. Sci. Mater. Electron. 26 (2015) 6366–6372.
[18] M.H. Wang, Z. Ma, H.G. Xue, S.P. Guo, Highly cycling stable $LiFeTiO_4$/CNTs composite as a cathode material for lithium-ion batteries, Inorg. Chem. Front. 5 (2018) 2306–2313.
[19] M.H. Pyun, Y.J. Park, Graphene/$LiMn_2O_4$ nanocomposites for enhanced lithium ion batteries with high rate capability, J. Alloy. Compd. 643 (2015) S90–S94.
[20] Y. Bao, X. Zhang, X. Zhang, L. Yang, X. Zhang, H. Chen, M. Yang, D. Fang, Free-standing and flexible $LiMnTiO_4$/carbon nanotube cathodes for high performance lithium ion batteries, J. Power Sources 321 (2016) 120–125.
[21] C.F.J. Francis, I.L. Kyratzis, A.S. Best, Lithium-ion battery separators for ionic-liquid electrolytes: a review, Adv. Mater. 32 (2020) 1–22.
[22] J. Han, K. Kim, Y. Lee, N. Choi, Scavenging materials to stabilize $LiPF_6$ -containing carbonate-based electrolytes for Li-ion batteries, Adv. Mater. 31 (2019) 1–12.
[23] G.A. Giffin, A. Moretti, S. Jeong, S. Passerini, Decoupling effective Li+ ion conductivity from electrolyte viscosity for improved room-temperature cell performance, J. Power Sources 342 (2017) 335–341.
[24] H. Zheng, H. Zhang, Y. Fu, T. Abe, Z. Ogumi, Temperature effects on the electrochemical behavior of spinel LiMn2O4 in quaternary ammonium-based ionic liquid electrolyte, (2005) 13676–13684.
[25] Q. Yang, Z. Zhang, X.G. Sun, Y.S. Hu, H. Xing, S. Dai, Ionic liquids and derived materials for lithium and sodium batteries, Chem. Soc. Rev. 47 (2018) 2020–2064.
[26] L. Zhao, Y.S. Hu, H. Li, Z. Wang, L. Chen, Porous $Li_4Ti_5O_{12}$ coated with N-doped carbon from ionic liquids for Li-ion batteries, Adv. Mater. 23 (2011) 1385–1388.
[27] X. Cui, Y. Li, S. Bachmann, M. Scalone, A.E. Surkus, K. Junge, C. Topf, M. Beller, Synthesis and characterization of iron−nitrogen-doped graphene, J. Am. Chem. Soc. 137 (2015) 10652–10658.
[28] S. Chauque, A.H. Braga, R.v. Gonçalves, L.M. Rossi, R.M. Torresi, Enhanced energy storage of Fe_3O_4 nanoparticles embedded in N-doped graphene, ChemElectroChem 7 (2020) 1456–1464.
[29] S. Chakrabarti, A.K. Thakur, K. Biswas, Raman and FTIR spectroscopy study of $LiFeTiO_4$ and Li_2FeTiO_4, Ionics 22 (2016) 2045–2057 (Kiel).
[30] V. Selvamani, N. Phattharasupakun, J. Wutthiprom, M. Sawangphruk, High-performance spinel $LiMn_2O_4$@carbon core-shell cathode materials for Li-ion batteries, Sustain. Energy Fuels 3 (2019) 1988–1994.
[31] C. Ramana, M. Massot, C.M. Julien, XPS and Raman spectroscopic characterization of $LiMn_2O4$ spinels, Surf. Coat. Technol. 37 (2005) 412–416.
[32] R. Chen, M. Knapp, M. Yavuz, R. Heinzmann, D. Wang, Reversible Li + storage in a $LiMnTiO_4$ spinel and its structural transition mechanisms, J. Phys. Chem. C 118 (2014) 12608–12616.
[33] R. Muzyka, S. Drewniak, T. Pustelny, M. Chrubasik, G. Gryglewicz, Characterization of graphite oxide and reduced graphene oxide obtained from different graphite precursors and oxidized by different methods using Raman spectroscopy, Materials 11 (2018) 15–17 (Basel).
[34] T. Wang, S. Kumar, Electrospinning of polyacrylonitrile nanofibers, J. Appl. Polym. Sci. 102 (2006) 1023–1029.
[35] C.A. Velásquez, F.A. Vásquez, M. Alvarez-Láinez, A. Zapata-González, J. A. Calderón, Carbon nanofibers impregnated with Fe_3O_4 nanoparticles as a flexible and high capacity negative electrode for lithium-ion batteries, J. Alloy. Compd. 862 (2021), 158045.
[36] X.J. Lee, B.Y.Z. Hiew, K.C. Lai, L.Y. Lee, S. Gan, S. Thangalazhy-Gopakumar, S. Rigby, Review on graphene and its derivatives: synthesis methods and potential industrial implementation, J. Taiwan Inst. Chem. Eng. 98 (2019) 163–180.
[37] Z. Sheng, L. Shao, J. Chen, W. Bao, F. Wang, X. Xia, Catalyst-free synthesis of nitrogen-doped graphene via thermal annealing graphite oxide with melamine and its excellent electrocatalysis, ACS Nano 5 (2011) 4350–4358.
[38] S. Dai, Z. Liu, B. Zhao, J. Zeng, H. Hu, Q. Zhang, D. Chen, C. Qu, D. Dang, M. Liu, A high-performance supercapacitor electrode based on N-doped porous graphene, J. Power Sources 387 (2018) 43–48.
[39] P. Bharathidasan, M.B. Idris, D.W. Kim, S.R. Sivakkumar, S. Devaraj, Enhanced capacitance properties of nitrogen doped reduced graphene oxide obtained by simultaneous reduction and nitrogen doping, FlatChem 11 (2018) 24–31.
[40] Y. Li, D. Pan, J. Xie, Z. Yan, Zhang Mingmae, Ultrafine Co_3O_4 embedded in nitrogen-doped graphene with synergistic effect and high stability for supercapacitor, RSC Adv. 6 (2016) 48357–48364.
[41] D. He, Z. Peng, W. Gong, Y. Luo, P. Zhao, L. Kong, Mechanism of a green graphene oxide reduction with reusable potassium carbonate, RSC Adv. 5 (2015) 11966–11972.
[42] H. Liu, J. Wang, X. Zhang, D. Zhou, X. Qi, B. Qiu, J. Fang, R. Kloepsch, G. Schumacher, Z. Liu, J. Li, Morphological evolution of high-voltage spinel $LiNi_{0.5}Mn_{1.\ 5}O_4$ cathode materials for lithium-ion batteries: the critical effects of surface orientations and particle size, ACS Appl. Mater. Interfaces 8 (2016) 4661–4675.
[43] S. Yang, X. Feng, S. Ivanovici, K. Müllen, Fabrication of graphene-encapsulated oxide nanoparticles: towards high-performance anode materials for lithium storage, (2010) 8586–8589.
[44] J. Zhang, Z. Huang, C. He, J. Zhang, P. Mei, X. Han, Binary carbon - based additives in $LiFePO_4$ cathode with favorable lithium storage, Nanotechnol. Rev. 9 (2020) 934–944.
[45] K. Ariyoshi, Y. Iwakoshi, N. Nakayama, T. Ohzuku, Topotactic two-phase reactions of $Li[Ni_{1/2}Mn_{3/2}]O_4$ (P4332) in nonaqueous lithium cells, J. Electrochem. Soc. 151 (2004) 296–303.
[46] V. Borgel, E. Markevich, D. Aurbach, G. Semrau, M. Schmidt, On the application of ionic liquids for rechargeable Li batteries: high voltage systems, J. Power Sources 189 (2009) 331–336.
[47] B. Deng, H. Wang, W. Ge, X. Li, X. Yan, T. Chen, M. Qu, G. Peng, Investigating the influence of high temperatures on the cycling stability of a $LiNi_{0.6}Co_{0.2}Mn_{0.2}O_2$ cathode using an innovative electrolyte additive, Electrochim. Acta 236 (2017) 61–71.
[48] R. Zarrougui, M. Dhahbi, D. Lemordant, Effect of temperature and composition on the transport and thermodynamic properties of binary mixtures of ionic liquid N-Butyl-N-methylpyrrolidinium bis(trifluoromethanesulfonyl)imide and propylene carbonate, J. Solution Chem. 39 (2010) 921–942.
[49] G.J. Brug, A.L.G Van Den Eeden, M. Sluyters-rehbach, J.H. Sluyters, The analysis of electrode impedances complicated by the presence of a constant phase element, 1984.
[50] S. Javadian, Z. Parviz, P. Salimi, M. Nasrollahpour, H. Gharibi, H. Kashani, A. Morsali, R.P. Zaccaria, Engineering cobalt-based nanoparticles encapsulated in hierarchical porous N-doped carbon as an efficient electrode for Li storage, J. Alloy. Compd. 898 (2022).
[51] S. Chauque, F.Y. Oliva, A. Visintin, D. Barraco, E.P.M. Leiva, O.R. Cámara, Lithium titanate as anode material for lithium ion batteries: synthesis, post-treatment and its electrochemical response, J. Electroanal. Chem. 799 (2017) 142–155.
[52] M. Luo, H. Yu, H. Lan, L. Yan, S. Qian, Synthesis and electrochemical characteristics of isostructural $LiMTiO_4$ (M = Mn, Fe, Co), Ceram Int. 43 (2017) 5728–5733.

[53] T.A. Ta, H.S. Nguyen, O.T.T. Nguyen, C.T. Dang, L.A. Hoang, L.D. Pham, Crystalline structure and electrical conductivity of nickel substituted spinel lithium manganese oxide, Mater. Res. Express 6 (2019).
[54] K. Rajagopalan, B. Ramasubramanian, S. Velusamy, S. Ramakrishna, A.M. Kannan, M. Kaliyannan, S. Kulandaivel, Examining the economic and energy aspects of manganese oxide in Li-Ion batteries, Mater. Circ. Economy 4 (2022).
[55] G. Cherkashinin, K. Nikolowski, H. Ehrenberg, S. Jacke, L. Dimesso, W. Jaegermann, The stability of the SEI layer, surface composition and the oxidation state of transition metals at the electrolyte-cathode interface impacted by the electrochemical cycling: x-ray photoelectron spectroscopy investigation, Phys. Chem. Chem. Phys. 14 (2012) 12321–12331.
[56] S. Jiao, X. Ren, R. Cao, M.H. Engelhard, Y. Liu, D. Hu, D. Mei, J. Zheng, W. Zhao, Q. Li, N. Liu, B.D. Adams, C. Ma, J. Liu, J.G. Zhang, W. Xu, Stable cycling of high-voltage lithium metal batteries in ether electrolytes, Nat. Energy 3 (2018) 739–746.
[57] J. Alvarado, M.A. Schroeder, M. Zhang, O. Borodin, E. Gobrogge, M. Olguin, M. S. Ding, M. Gobet, S. Greenbaum, Y.S. Meng, K. Xu, A carbonate-free, sulfone-based electrolyte for high-voltage Li-ion batteries, Mater. Today 21 (2018) 341–353.
[58] D.M. Piper, T. Evans, K. Leung, T. Watkins, J. Olson, S.C. Kim, S.S. Han, V. Bhat, K. H. Oh, D.A. Buttry, S.H. Lee, Stable silicon-ionic liquid interface for next-generation lithium-ion batteries, Nat. Commun. 6 (2015) 1–10.
[59] X.Q. Zhang, X. Chen, L.P. Hou, B.Q. Li, X.B. Cheng, J.Q. Huang, Q. Zhang, Regulating anions in the solvation sheath of lithium ions for stable lithium metal batteries, ACS Energy Lett. 4 (2019) 411–416.
[60] T. Evans, D.M. Piper, H. Sun, T. Porcelli, S.C. Kim, S.S. Han, Y.S. Choi, C. Tian, D. Nordlund, M.M. Doeff, C. Ban, S.J. Cho, K.H. Oh, S.H. Lee, *In situ* engineering of the electrode–electrolyte interface for stabilized overlithiated cathodes, Adv. Mater. 29 (2017) 1–7.